# Multifunctionality of Layered Materials

Septiany, Liany

*DOI:*
10.33612/diss.182500502

# Chapter 1

# General Introduction

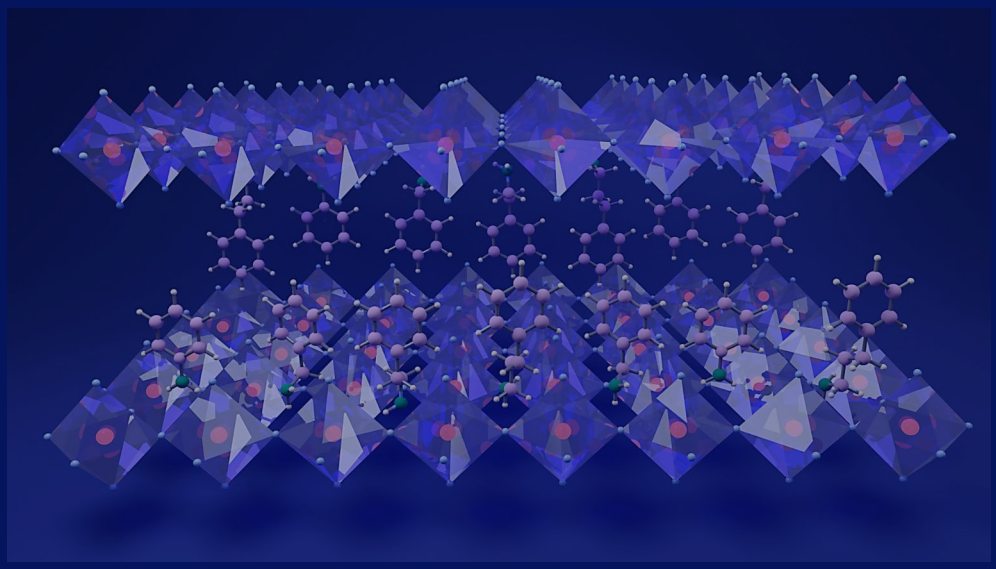

Layered materials are known for their multifunctionality. In this thesis, we use the term "layered materials" to describe compounds that possess relatively strong chemical bonding in two dimensions, while the layers are separated by a distance significantly larger than typical interatomic spacings such that bonding in the out-of-plane direction is much weaker. The physical properties are then mainly determined by the nature of the planes in which the main connectivity lies. In the work presented in this thesis we divide such layered materials into two different categories, consisting of either (i) all-inorganic compounds or (ii) hybrid organic-inorganic compounds.

In the first category, a class of bulk two-dimensional (2D) all-inorganic compounds is introduced - the family of IV-VI semiconductors. These materials are known for their promising applications in fields such as nanoelectronics, optoelectronics, and energy harvesting. They have recently gained a lot of attention for their thermoelectric properties, which is largely due to the fact that their layered structure promotes ultra-low thermal conductivity that is favorable for thermoelectric applications.

In the second category, layered hybrid organic-inorganic perovskites have also gained a lot of interest in recent years. While their 3D counterparts tend to be chemically unstable in ambient conditions and for which the choice of organic cations is limited, 2D hybrid perovskites exhibit greater freedom in both aspects. 2D hybrid perovskites are already known for their excellent optoelectronic properties, which can for example be applied in solar cells, light-emitting diodes (LEDs) and photodetectors. Here we focus on some other aspects of these materials, namely on their structural, magnetic, and magnetocaloric properties.

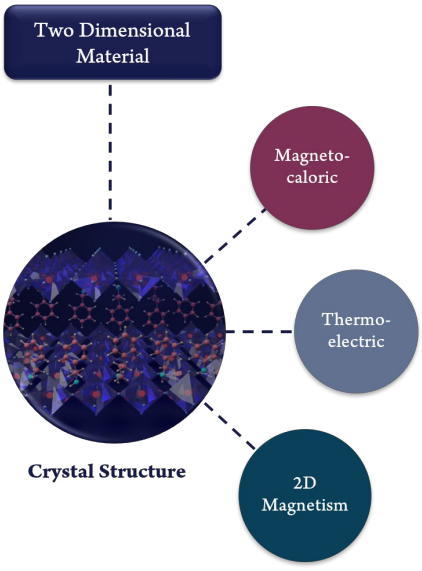

## 1.1 Multifunctionality of Layered Materials

Layered materials are known to possess a great variety of physical properties.[1–6] They have perhaps been most widely studied for their optoelectronic applications.[7–11] For example, 2D hybrid perovskites are of particular interest for photovoltaic (PV) applications due to their excellent environmental stability in PV devices compared to 3D perovskites. However, optoelectronic properties are not the focus of this thesis and will not be further discussed here. Instead, we concentrate on the unique thermal, magnetic and electrical properties shown by layered materials that are not found in 3D materials. Here it is essential to better understand the relationships between structure and physical properties in layered materials, some aspects of which are outlined below.

### 1.1.1 Thermoelectric Properties

The thermoelectric effect has been gaining increasing attention due to the high demand for renewable energy sources and more efficient use of existing sources. Thermoelectric power generation technology has been used for powering the spacecraft of several NASA deep-space missions.[12] However, the commercial use of thermoelectric materials has in general been limited to niche applications, although there is growing interest in waste-heat recovery. Automotive exhaust, home heating, and industrial processes generate enormous quantities of waste heat that can be partially converted to electricity. This is performed in thermoelectric devices by employing a temperature difference to induce charge carrier flow in a semiconductor. A typical thermoelectric module shown in Fig. 1.1. Thermoelectric generators are solid-state devices that have no moving parts, and are scalable and reliable. However, the active materials used for this application are often lead (Pb)-based and also incorporate high concentrations of scarce elements, particularly tellurium (Te). Thus, the development of high-performance thermoelectric materials comprised of earth-abundant elements with low toxicity has become an important challenge.

The performance of thermoelectric materials is often quantified by the figure of merit (ZT). Materials with ZT > 1 are potentially viable for use in waste-heat recovery applications. The ZT value is defined as follows:

$$ZT = \frac{S^2 \sigma T}{\kappa} \tag{1.1}$$

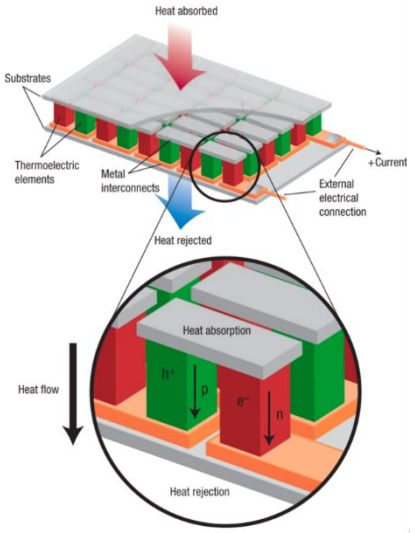


***Figure 1.1*** *Thermoelectric module consisting of p- and n-type semiconductors (figure adapted from ref. [14])*

Here S is the Seebeck coefficient, $\sigma$ is the electrical conductivity, $\kappa$ is the thermal conductivity, and T is the temperature. In order to achieve a high ZT, the thermal conductivity must be minimised and/or the power factor (PF) should be maximised, where PF = $S^2\sigma$.[13] A reduction in thermal conductivity can be realized by strengthening the phonon scattering by defect engineering, control of the nanostructure/microstructure, and/or searching for materials with unique vibrational modes that lead to intrinsically low thermal conductivity. Meanwhile, enhancing the power factor can be achieved by band-structure engineering and/or by carrier concentration optimization.[14–17] Band structure engineering can be performed either by modifying the relative energies of the electronic bands through alloying[18,19] or by introducing impurity energy levels through resonant doping.[20,21] Optimizing both approaches independently is in practice difficult due to the complex correlation between the thermal and electrical properties. For example, increasing the carrier concentration improves the electrical conductivity but reduces the Seebeck coefficient; in addition, the thermal conductivity will also increase.

A common approach that has been followed in recent years is to use metallic materials or heavily-doped semiconductors and to nanostructure them or introduce point defects to decrease their thermal conductivity. Alternatively, materials with intrinsically low thermal conductivity can

be chosen and modified by band structure engineering via doping processes. Overall, competitive TE materials require a synergistic combination of low $\kappa$ for sustaining a sizeable thermal gradient, high $\sigma$ for suppressing Joule heating loss, and large S for enhanced voltage output in the generator.

More in-depth strategies for maximizing ZT at a constant doping level include increasing the band degeneracy[22] (also known as band convergence[19]) by tuning the crystal structure, enhancing the band effective mass (by introducing resonant levels[20,23] or achieving band flattening), improving the carrier mobility (by modulation doping or texturing), and decreasing the lattice thermal conductivity (by synergistic alloying[24], second-phase nanostructuring,[25,26] mesostructuring, or designing multi-length-scale hierarchical architectures). Some of these challenges are described in more detail below.

#### 1.1.1.1 Electrical Transport

A large PF is desired for good thermoelectric performance. Here both *S* and σ are correlated with the carrier concentration of the material. To ensure a large Seebeck coefficient, only a single type of charge carrier should be present and the carrier concentration should not be too high. However, a low carrier concentration results in low electrical conductivity. Fig. 1.2 shows that the value of ZT reaches a maximum where a compromise is found between the Seebeck coefficient and the electrical conductivity, usually at carrier concentrations in the range $10^{19}$-$10^{20}$ $cm^{-3}$.[23,27] These values of carrier concentration are commonly found in heavily doped semiconductors. However, the carrier concentration is not constant over an extended temperature range; therefore, an optimum carrier density stabilization should be employed, such as gradient doping throughout the material.

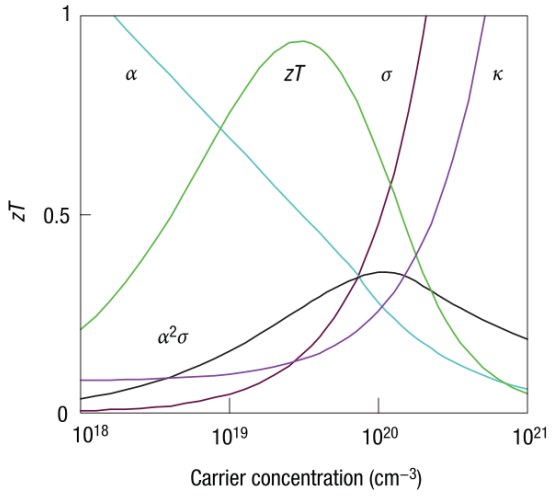


***Figure 1.2*** *ZT value as a function of carrier concentration (figure adapted from ref. [14])*

Another parameter related to the electrical transport of a material is the effective carrier mass, but in similar fashion to the Seebeck coefficient, effective mass ($m^*$) has a conflicting relation with the electrical conductivity ($\sigma$). A large $m^*$ gives a large Seebeck coefficient which is correlated with a low carrier concentration (n) as shown in Eq. 1.2 and 1.3. As the effective inertial mass ($m_I^*$) is also related to the mobility ($\mu$) as shown in Eq. 1.4, heavy carriers will move more slowly, therefore with lower mobility, which leads to low electrical conductivity.[16] The exact relationship between the effective mass and mobility depends on various aspects such as the electronic structure, carrier scattering mechanism, and anisotropy (which arises mainly from the crystal structure). High mobility and low effective mass are usually found in materials with small electronegativity differences. In contrast, high effective mass and low mobility are found in narrow band materials, such as ionic compounds.

$$S = \frac{8\pi^2 k_B^2 T}{3qh} m^* \left(\frac{\pi}{3n}\right)^{2/3} \quad (1.2)$$

$$\sigma = n.e.\mu \quad (1.3)$$

$$\mu = \tau e / m_I^* \quad (1.4)$$

Approaches to maximize the PF have been employed by carefully tailoring the electronic band structure, for example by manipulating the number of band extrema, also known as valley degeneracy ($N_v$), as well as the carrier effective mass ($m_b^*$)).[22] $N_v$ is strongly dependent on the crystal symmetry and can be large when the crystal structure is highly symmetric. Another approach to increasing the effective $N_v$ is to bring different bands in the Brillouin zone towards convergence, with just a small difference in energy. The effective mass $m_b^*$ in a band is related to the curvature of the band and can thus be modified by distorting the band. Two common strategies to increase $m_b^*$ are by band flattening and by introducing resonant levels through chemical doping.[22] Band flattening can be achieved through doping, introducing highly localized orbitals that can decrease the overall degree of orbital overlap. Resonant levels originate from coupling between the electrons of a dilute impurity with those of the conduction or valence band of the host solid. This creates an excess density of states near the resonant energy and can give rise to improved $m_b^*$ and an enhanced Seebeck coefficient if the Fermi level can be brought close in energy. It should be noted that generally, an increase in $m_b^*$ will result in a decrease in carrier mobility and thus electrical conductivity as described above. However, the carrier mobility will be decreased to a lesser extent by increasing $N_v$ than by increasing $m_b^*$. Note that several different types of effective mass have been introduced in this discussion. Although in general the effective mass can be considered as a fundamental property of a material, the precise definition depends on the purpose for which it is used. Here we refer to $m^*$as the general effective mass, $m_b^*$ is used in relation to the band structure (the band effective mass), and $m_I^*$ is the effective inertial mass (used to describe the mobility of the carriers).

#### 1.1.1.2 Thermal Transport

The thermal conductivity of a material has two main contributions and can be expressed as $\kappa = \kappa_e + \kappa_l$ , where $\kappa_e$ is the electronic contribution and $\kappa_l$ the lattice contribution. The electronic contribution represents the transport of heat by electrons and holes, while the lattice component arises from thermal transport associated with phonons. The electronic contribution is directly related to the electrical conductivity by the Weidemann-Franz law, $\kappa = L\,\sigma\,T$, where L is the Lorentz number, $\sigma$ is the electrical conductivity and T is the temperature. Good thermoelectric

materials are usually crystalline, thus the phonons can be scattered without significantly disrupting the electrical conductivity. Heat flow is mediated by a spectrum of phonons covering a range of wavelengths and mean free paths (from less than 1 nm to greater than 10 μm), which requires scattering agents with various length scales.

Three general strategies to reduce $\kappa_l$ have been proposed in the literature.[15–17] First, the introduction of imperfections in the host lattice by doping or alloying is a well-established approach. This can be achieved by introducing point defects, for example by site substitution (doping/alloying) with isoelectronic elements to preserve the electronic structure while creating significant mass contrast to disrupt the phonon path, or by creating vacancies. The second strategy is to use a complex crystal structure; for example, so-called rattling structures like skutterudites contain atoms in large cages that are weakly bonded and have large amplitudes of vibration. The third approach is to scatter phonons at interfaces, which can be introduced via structural inhomogeneities such as composite materials where the phases are mixed on the nanometer scale. For example, the microstructural / nanostructural complexity in the TAGS and LAST families of thermoelectrics may be largely responsible for their high ZT values.[21]

Other approaches include searching for materials with intrinsically low thermal conductivity. The rational design of such materials often employs the concepts of low dimensionality, low phonon velocity, large anharmonicity, and low specific heat.[15] Recently, 2D materials with intrinsically layered structures held together by the van der Waals force have attracted widespread attention due to their low $\kappa_l$.[5,24,28,29] For example, SnSe exhibits ultralow thermal conductivity resulting from its layered structure combined with large phonon anharmonicity associated with the bonding arrangement.[30,31]

### 1.1.2 Magnetocaloric Effect

The magnetocaloric effect (MCE) is an intrinsic property of magnetic (usually ferromagnetic) materials. When an external magnetic field is applied under adiabatic conditions, the spins will tend to align with the field, decreasing the magnetic entropy and inducing a corresponding increase in lattice entropy, resulting in a temperature increase ($\Delta T_{ad}$). Alternatively, under

isothermal conditions the MCE will involve an entropy change ($\Delta S_{iso}$) on application of an external magnetic field.[32–34] The magnetocaloric effect is of interest as an alternative technology for refrigeration applications ranging from ambient temperature to liquid helium temperature. Apart from maximizing $\Delta T_{ad}$ and $\Delta S_{iso}$, for which materials with a high saturation magnetization are often suitable, another useful parameter related to the efficiency of a magnetocaloric material is the relative cooling power (RCP). The RCP quantifies the heat transfer between the hot and cold reservoirs in one refrigeration cycle. The MCE reaches its largest value close to the critical temperature of a (ferro)magnetic transition due to the spontaneous ordering of magnetic spins, i.e., effective spin-lattice coupling. Traditional magnetocaloric compounds exhibit a first-order magnetic transition with respect to temperature or applied field, but they suffer from chemical and physical instabilities such as thermal and magnetic hysteresis. Studies have thus become more focused on materials with second-order magnetic transitions. Here, the low coercivity keeps heat losses associated with the transition to a minimum. The magnitude of the isothermal magnetic entropy change ($\Delta S_m$) can be calculated from the Maxwell relation and when determined using magnetometry measurements can be expressed as:

$$\Delta S(T,H) = \int_0^H \left(\frac{\partial M}{\partial T}\right)_H dH \tag{1.5}$$

Meanwhile, the RCP can be determined as:

$$RCP = |\Delta S_M^{Max}|\ x\ \delta T_{FWHM} \tag{1.6}$$

Here $\delta T_{FWHM}$ is defined as the full-width at half maximum of the magnetic entropy change peak obtained from a Gaussian fit of the $\Delta S_m$ vs T curve.

### 1.1.3 Two-dimensional Magnetism

Layered organic-inorganic perovskites containing transition metals on the perovskite B-site have been used extensively as ideal systems in which to study two-dimensional magnetism. Generally, the interlayer exchange coupling interaction is a factor of up to $10^{-6}$ weaker than the intralayer coupling; [35,36] thus, the interlayer coupling is often considered negligible. Theoretically, a 2D magnet should not undergo any phase transition associated with long-range ordering. However,

in most 2D layered perovskites, the interlayer interaction cannot be neglected at low temperature and long-range magnetic ordering is often observed.[37–40]

In hybrid perovskites, there are no direct metal-metal contacts. The in-plane magnetic interaction arises from the M-X-M superexchange pathway, the strength and sign of which is determined by structural parameters such as bond lengths and bond angles. The presence of Jahn-Teller (JT) active metal cations such as $Cu^{2+}$ ($d^9$) leads to the situation of partial occupancy of degenerate d-orbitals, where the degeneracy is lifted by distortion of the $MX_6$ octahedra, which in most cases become elongated. The long axes of the octahedra lie in the plane of the inorganic layers; the elongated M-X bonds are arranged in an antiferrodistortive manner, with minimal overlap between adjacent half-filled (magnetic) $d_{x^2-y^2}$ orbitals which are nearly orthogonal to each other in the case of $Cu^{2+}$ as shown in Fig. 1.3. In this situation the superexchange that occurs via the p-orbital of the intermediate halide anion is weak and ferromagnetic. The interlayer interaction strength depends on the length of the organic spacer; however, the experimentally determined transition temperatures associated with long-range ordering have been found to show little correlation with the length of the spacer. [41]

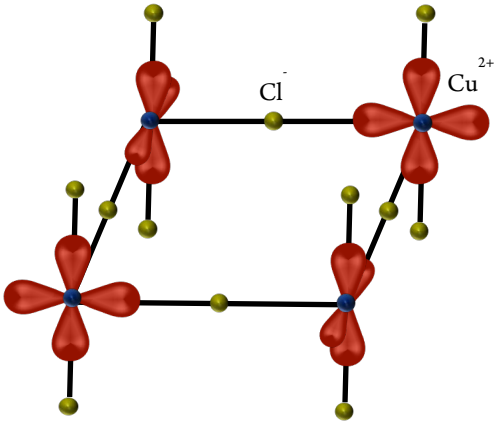


***Figure 1.3*** *Orbital arrangement in $Cu^{2+}$ hybrids.*

On the other hand, $Mn^{2+}$ and $Fe^{2+}$ ions, which do not exhibit JT distortion, give antiferromagnetic ordering in 2D hybrid perovskites. In these compounds the magnetic orbitals have the same orientation on adjacent metal sites, and according to the Goodenough-Kanamori rules for perovskites, this leads to strong antiferromagnetic superexchange.[42–44] The interlayer coupling depends on several factors such as the interlayer distance, the geometry of the bridging B-X-B linkage, and the type of halide ions (X).[45] The interlayer coupling is expected to decrease as the distance increases. Antiferromagnetic ordering in 2D materials gives rise to a distinct broad peak in the magnetization versus temperature curve above the long-range ordering temperature.

## 1.2 Layered Materials

Layered materials represent a large class of compounds that is constantly growing in number. They include, among others, graphene, transition metal dichalcogenides, and clay minerals, as well as hybrid organic-inorganic compounds. The 2D structures can often be obtained in either bottom-up fashion by self-assembly of the atoms/ions/molecules, or in top-down fashion by nano-structuring and exfoliation techniques. Below, we provide a brief explanation of the two types of layered materials investigated in this thesis, namely layered IV-VI compounds and layered organic-inorganic perovskites.

### 1.2.1 IV-VI Compounds

The family of IV-VI compounds can be synthesized from elements in columns IV (Ge, Sn, and Pb) and VI (S, Se, and Te) of the periodic table. Lead chalcogenides are among the oldest known narrow bandgap semiconducting materials; PbS, PbSe, and PbTe have been used for decades in electronic, thermoelectric and optical devices.[46] However, there is now an effort to replace lead in these compounds due to its toxicity. Regarding thermoelectric (TE) applications for converting heat to electrical energy, PbTe[47–51], SnSe[52–55], GeTe[56–58], and $Bi_2Te_3$[59,60] have been studied extensively by both theoretical and experimental approaches. Most compounds composed of group IV-VI elements, regardless of their crystal structure which can be 3D rocksalt-type or 2D layered, show excellent TE performance due to their intrinsically low thermal conductivity[27,29] and complex band structures[18,61]. The low thermal conductivity has been associated with anharmonic effects due

to resonant bonding[30,62] and/or lone pairs[63,64]. This is particularly the case in IV-VI materials with layered structures such as orthorhombic SnSe, for which the ultra-low thermal conductivity results in the best reported thermoelectric performance for a bulk material.[31] It is expected that other compounds in the IV-VI family with similar structures might possess comparable thermoelectric properties. Furthermore, the excellent performance of the IV-VI compounds can be partly explained by the effective mass tensor of the relevant charge carriers as determined by optical reflectivity and electrical transport measurements. This anisotropy is reflected in high Seebeck coefficients due to a large density-of-states effective mass, and high electrical conductivity due to a small conductivity effective mass.[65]

The excellent thermoelectric properties of various IV-VI compounds has attracted attention to the nature of the chemical bonding in these materials. A map created to classify binary chalcogenides based on their bonding properties (metavalent or covalent) is shown in Fig. 1.4. Metavalent bonding is described as resonance bonding, but is different to the π-bonding found in organic systems. Metavalent materials exhibit characteristics of both localized and delocalized electrons, as found in covalent and metallic bonding, respectively. They exhibit a large dielectric constant $\varepsilon^{\infty}$, high effective coordination numbers, and large Born effective charges $Z^{*}$. Almost all materials with a thermoelectric figure of merit $ZT > 0.7$ (yellow circles) belong to the red metavalent bonding region in Fig. 1.4. This observation shows that chemical bonding plays an important role in determining the transport properties of the IV-VI family of compounds.

The IV-VI compounds possess different crystal structures due to differences in the contributions of covalent, ionic, and metallic bonding; thus, a rich polymorphism exists. The crystal structures vary from the high symmetry cubic rocksalt structure to rhombohedral and low symmetry orthorhombic structures with decreasing ionic contribution to the bonding. The lead chalcogenides (PbS, PbSe, PbTe, SnTe) all adopt the NaCl structure in which each atom is octahedrally coordinated by six atoms of the other type. GeTe crystallizes in a distorted rocksalt structure belonging to the rhombohedral crystal system. The distortion arises from non-equal shifts of the cation and anion planes along the [111] direction, breaking inversion symmetry. GeS, GeSe, SnS, and SnSe possess a puckered layered structure similar to black phosphorus, which belongs to the

orthorhombic crystal class with space group Pnma, except for SnSe which adopts the Cmcm space group. The orthorhombic structure contains eight atoms and two adjacent double layers in the primitive unit cell. One atom in a single layer is connected to three nearest neighbours, which leads to the formation of zigzag chains, as shown in Fig. 1.5. Theoretical studies have predicted that GeS, GeSe, and SnS show similar thermoelectric properties to SnSe with large Seebeck coefficients, low thermal conductivity, and high power factor, which are the main properties required to realize optimal thermoelectric performance.[4,66–69] However, thus far the experimental results reported for these materials are not in good agreement with the predictions.[70,71]

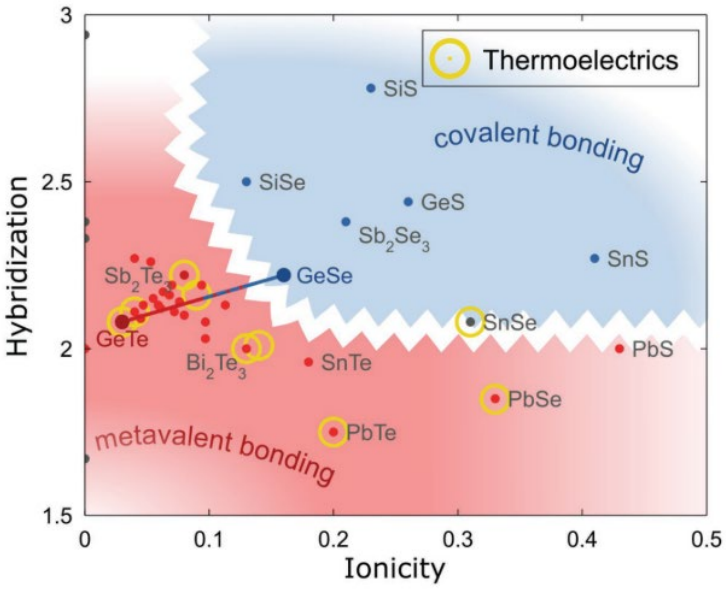


***Figure 1.4*** *Chemical bonding map for various chalcogenide compounds. The red region contains compounds that possess metavalent bonding, while the blue region is for compounds with covalent bonding. The yellow circles correspond to known thermoelectric materials with ZT > 0.7. (figure adapted from ref[65])*

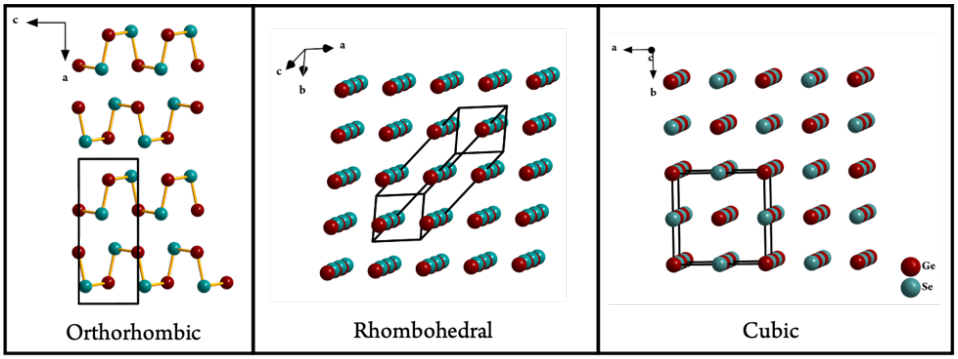


***Figure 1.5*** *Schematic of orthorhombic (space group Pnma), rhombohedral (R3m) and cubic (Fm-3m) crystal structures of GeSe.*

In Ge-chalcogenides, both rhombohedral and orthorhombic structures are found. The high symmetry rhombohedral phases exhibit good thermoelectric performance,[72] while the low symmetry orthorhombic phases show limited electrical conductivity,[70] preventing a large figure of merit from being reached. The distorted octahedral coordination in chalcogenides with the rhombohedral phase involves metavalent bonding. The symmetry leads to a large degeneracy of the valence band valleys; in addition, weak s-p hybridization and a small degree of charge transfer lead to strong band anisotropy. Both of these effects enhance the power factor of the rhombohedral phase, which behaves like a degenerate semiconductor.[65] This shows the importance of the relationship between chemical bonding, crystal structure and band structure.

The IV-VI compounds have quite different structural, electronic, and optical properties compared to other narrow gap semiconductors. The unique structure arises from the ten valence electrons per atomic pair instead of the eight valence electrons typical for the tetrahedrally bonded group IV, III-V, and II-VI semiconductors. The six p-electrons per atom pair in IV-VI compounds promote six-fold coordination in the lattice. Because there are only six p-electrons per atom pair, and yet there are six nearest neighbors for each atom, the precise electronic configuration plays an important role. This configuration can lead to both covalent and metallic bonding depending on the electronegativity of the atoms and their orbital hybridization. [65] The band gap in binary IV-VI chalcogenides is direct for the cubic structures and indirect for the orthorhombic phases. In the cubic structure there is no hybridization between the s and p-bands; the s-states are fully occupied

and only partly contribute to the bonding, while the p-band is half-filled and a very small band gap arises between the occupied and unoccupied levels. In contrast, for the orthorhombic structure the possibility of forming sp-hybridized orbitals is high and strongly covalent bonds are achieved. The strong sp-hybridization promotes splitting between the bonding and antibonding states, thus increasing the band gap.[73] The maximum of the valence band and the minimum of the conduction band do not cross the Fermi energy level for any compound, which is evidence of their narrowband semiconducting behaviour. The top of the valence band is mainly composed of the p-states of the group VI element, whereas the main contribution to the bottom of the valence band is the group IV element s-state. Mixed VI-s and VI-p orbitals contribute to the conduction band in both the cubic and orthorhombic phases.[22,65]

### 1.2.2 Layered Hybrid Organic-Inorganic Perovskites

The 3D perovskite structure has long been known and is named after the mineral $CaTiO_3$. Perovskites have a general formula of $ABX_3$, where A and B are cations and X is an anion. The $ABX_3$ structure is built by a corner-shared network of $BX_6$ octahedra, where the A cation occupies the cuboctahedral site between eight octahedra, shown in Fig. 1.6. If the A-site cation is a small monovalent organic cation, perovskite structures can be stabilized when X is a halide anion, and the resulting materials are often known as hybrid organic-inorganic perovskites. These halide perovskites have distinctive properties that derive from their relatively soft lattices and often dynamically disordered (with respect to the A-site cation) crystal structures.[74,75] Like a "normal" inorganic perovskite, hybrid perovskites can only be formed by choosing cations and anions of appropriate size, which should obey the Goldsmith tolerance factor:

$$t = \frac{r_A + r_X}{\sqrt{2}\,(r_B + r_X)} \tag{1.7}$$

where $r_A$, $r_B$, and $r_X$ are the ionic radii. When t is in the range of ~0.8-1, a stable 3D perovskite can be formed.[76] In hybrid organic-inorganic perovskites, the B cations are usually transition metal or group 14 cations, while a halide anion ($Cl^-$, $Br^-$ or $I^-$) occupies the X site.

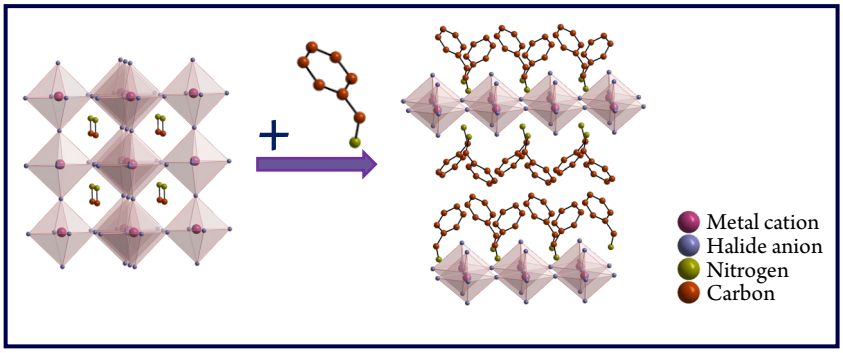


***Figure 1.6*** *Tailoring dimensionality in hybrid perovskites*

To obtain a tolerance factor in the perovskite range, only small A-site cations are suitable, such as methylammonium ($CH_3NH_3$) and formamidinium ($CH(NH_2)_2$). The B-site cations should be relatively large, such as $Pb^{2+}$ and $Sn^{2+}$. These hybrid perovskites tend to be unstable under standard environmental conditions and undergo decomposition. Due to this drawback, researchers have increasingly been looking at 2D hybrid perovskites, which generally contain larger organic cations and have better stability and structural tunability compared to the 3D perovskites. The higher stability towards environmental conditions is mainly due to the increased influence of the organic cations which provide a steric barrier for surface water adsorption and suppress the intrusion of moisture due to their hydrophobicity.[77]

The dimensionality of a perovskite is determined by the connectivity of the metal-halide octahedra.[2,41,45,78–80] Three types of inorganic octahedral connectivity modes have been experimentally observed, consisting of corner-sharing, edge-sharing, and face-sharing octahedra. The way that individual octahedra are linked determines the orbital overlap between the metal and the halide, which generally influences the bandgap of the compound. Corner-sharing provides the most robust type of bonding between the metal and halogen, and this type of connectivity is found in the materials studied in this thesis.

The organic cation must contain terminal functional groups that can interact with the anionic inorganic substructure. Most known layered (2D) perovskite derivatives feature mono- or diammonium cations, leading to various hydrogen bonding patterns that connect the cation to the

inorganic substructure. The hydrogen bonding pattern can also determine the orientation and conformation of the organic cations. Moreover, functional organic cations can also distort the inorganic framework, as reported for compounds containing aromatic groups with $\pi$-systems.[81–83] The distortion of the inorganic lattice can alter the physical properties. The characteristics that determine the suitability of the organic cation as a spacer are (i) its net positive charge at the anchoring position and degree of substitution, (ii) its hydrogen-bonding capacity, (iii) its stereochemical configuration (i.e., aliphatic, aromatic, or functionalized), and (iv) its space-filling ability (linear or branched).[2] If the cation is too large or too bulky, the inorganic lattice will adapt and form alternative structures with lower dimensionality. The octahedral connectivity can also change from corner-shared to either an edge-shared or face-shared network, or a combination of these.

The layered perovskites studied herein have a general formula of $(A')_m(A)_{n-1}B_nX_{3n+1}$, where A' can be a mono- or divalent organic cation that forms a bilayer (m = 2) or monolayer (m = 1) respectively, acting as a spacer between the inorganic sheets of $(A)_{n-1}B_nX_{3n+1}$ which contain small A cations such as methylammonium for n > 1. The metal halide sheet has a thickness of n octahedra, which for n > 1 can be viewed as a slab from the 3D perovskite lattice; the thickness can be adjusted by tuning the precursor composition, where n = ∞ corresponds to a 3D perovskite, while n = 1 represents a pure 2D perovskite and $1 < n \leq 5$ are known as quasi-2D. The orientation of the slab is determined by the geometry and noncovalent bonding interactions of the templating organic cation. Structures have been reported in which the slab is (100)-oriented, (110)-oriented, and (111)-oriented with respect to the perovskite unit cell. Perovskites with (110)- and (111)- oriented inorganic layers are much more scarce. Generally, they exhibit corrugated layers where the layers are shifted along the a- and/or b-axes by one half of a unit cell. The (110)-oriented perovskite layers are intrinsically highly distorted, and are often stabilized by site-specific hydrogen bonding or by other secondary bonding interactions. A set of defective perovskites with B-site deficiency belongs to the (111)-oriented perovskite class. Various types of layered perovskite are given in Fig. 1.7.

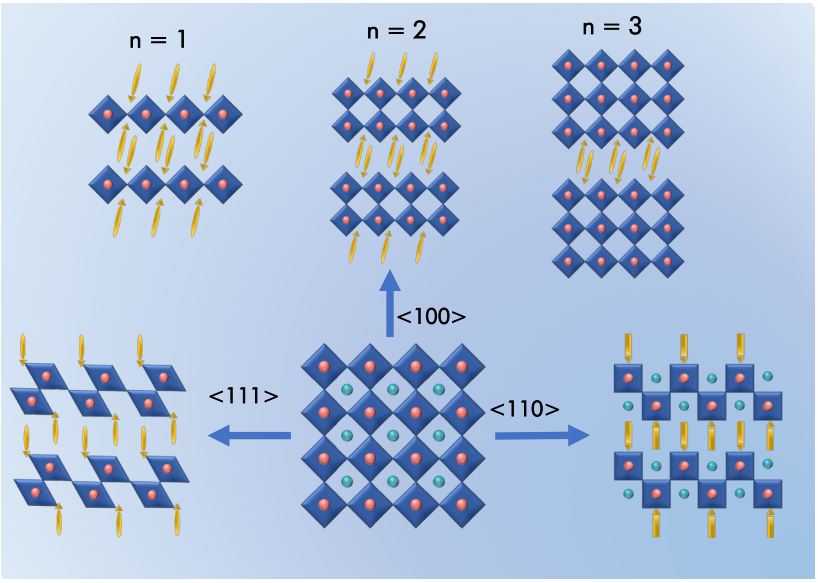


***Figure 1.7*** *Various types of layered hybrid perovskites with different values of n and different orientations of the octahedral slabs.*

The studies described in this thesis focus only on the most commonly observed type of layered perovskites, which are (100)-oriented and have a molecular formula of $A'_2A_{n-1}B_nX_{3n+1}$. Unlike the other types, the (100)-oriented class is tolerant of a broad range of organic cations and inorganic components, leading to a high degree of compositional diversity. This class can be further divided into three categories: the Ruddlesden-Popper (RP) phases, Dion-Jacobson (DJ) phases, and Aurivillius phases.[2] The difference between the RP and DJ phases lies in the organic cation that they possess. In RP phases, a monoammonium organic cation is used, leading to a chemical formula of $A'_2A_{n-1}B_nX_{3n+1}$, while in DJ phases with composition $A'A_{n-1}B_nX_{3n+1}$ a diammonium organic cation is used. Aurivillius phases contain excess anion species with a chemical formula of $A'_2X_2A_{n-1}B_nX_{3n+1}$.[84–86] In this thesis, we focus on (100)-oriented layered perovskites of the RP type with n = 1, which gives compounds with the chemical formula $A_2BX_4$.[2,41,45]

Layered hybrid perovskites usually consist of earth-abundant and low-cost elements, and are easy to synthesize; for example, single crystals can often be grown from solution at temperatures of ~100 °C under ambient conditions. Crystals result from the self-assembled stacking of the organic and inorganic constituents. The organic molecules template the formation of the inorganic

sublattice from the metal and halide ions in solution, and the inorganic part largely determines the physical properties that the resulting compound may possess. These hybrid materials combine the synthetic tunability of small organic molecules with the electronic diversity of extended inorganic solids. Not every combination of metal cation and halide anion is possible due to size mismatch and redox instability, among other reasons. A wide range of divalent cations, including transition metal and group 14 cations, has been incorporated on the B-site of 2D perovskites, such as $Sn^{2+}$, $Pb^{2+}$, $Cu^{2+}$, $Mn^{2+}$ and $Fe^{2+}$. The perovskite structure is also highly tolerant to various organic functional groups. Furthermore, the length of the organic molecule can vary widely from the shortest possible, $(CH_3NH_3)^+$, to a long cation such as $(C_{18}H_{37}NH_3)^+$.[87,88] Thus, 2D perovskites show great structural versatility.

Layered perovskite derivatives featuring primary ammonium cations tend to have distorted inorganic layers with the B-X-B angles ranging from 140 to 160° (compared to 180° for an undistorted layer). Several structural parameters play a role in determining the degree of distortion. The B-X-B angles are associated with rotations of the relatively rigid $BX_6$ octahedra, which can have out-of-plane and in-plane components. These rotations are caused either by interactions between the halide anions of the inorganic layers and the hydrogens of the ammonium functional groups, or by stereochemical activity of the B-site cation lone pairs, which is also reflected in the X–B–X bond angles within a given $BX_6$ octahedron.[45] In the perovskite structure, a stereochemically active lone pair on the B-site cation (or s-orbital hybridization) generally gives rise to a shift away from the crystallographic center of the metal halide octahedron, resulting in an alternating pattern of long-and-short B-X bonds. For hybrid perovskites, the directional hydrogen bonding involving the organic cation can also couple through intervening halogen anions to the stereochemically active $s^2$ electron pair, giving rise to a coordinated structural distortion. [45]

2D hybrid perovskites offer a much larger playground than their 3D counterparts for chemists to investigate their fundamental structure-property relationships. Reducing the dimensionality of a three-dimensional (3D) crystal lattice can yield wholly new physical phenomena. For example, breaking the 3D connectivity of the inorganic lattice by employing large organic molecules affords atomically smooth organic-inorganic interfaces and produces

dimensional confinement in bulk materials, as shown in Fig. 1.6. The organic cations can act as an insulating barrier that confines the charge carriers in two dimensions. In two dimensions, the inherent liquid-like dynamic disorder of such perovskites blends with the weak dispersion forces governing the crystal packing of the organic spacers, producing a genuinely hybrid material.[74,75] Reports have shown a wide variety of interesting and important properties, such as soft and dynamic structures,[89] strong anisotropy,[90] high photoluminescence quantum yield,[91] strongly bound excitons at room temperature,[92] large Rashba splitting,[93,94] ferroelectricity,[95] and 2D magnetism.[35,96] Layered hybrid perovskites have demonstrated breakthrough performance in solar cells,[97] light-emitting diodes (LEDs),[98] and photodetectors.[99] Beyond the field of photovoltaics in which a large proportion of the research on 2D hybrid perovskites is currently found, their exceptionally high degree of structural flexibility, excellent optoelectronic properties, and ease of fabrication could enable applications in photodetectors, LEDs, batteries, and solid-state lighting applications. In addition, there are several reports of exciting multiferroic[81,100–102] and nonlinear optical properties[103] of hybrid perovskites. The full potential of the broad class of 2D hybrid perovskites in these applications is just starting to be uncovered.

## 1.3 Outline of Thesis

In this thesis, the structural and physical properties of bulk layered materials are studied. The connectivity is distinct from their 3D counterparts and gives rise to interesting physical properties, some of which are addressed in chapters 3-6. The content of this thesis is as follows.

**Chapter 2** explains various synthesis and measurement techniques used in this thesis. The synthesis part covers the solid-state reaction technique used to obtain the IV-VI compounds, as well as crystallization techniques used to obtain single crystals of layered organic-inorganic perovskites. This is followed by an overview of the measurement techniques that were used to obtain insight into their structural and physical properties. The structural properties were studied using a combination of X-ray diffraction and scanning electron microscopy. The chemical compositions and phase transitions of the materials were studied using energy dispersive X-Ray spectroscopy (EDS) and differential scanning calorimetry (DSC) / thermogravimetric analysis (TGA). Various instruments were used to study an array of physical properties. A laser flash apparatus was used to determine the

thermal conductivity and heat capacity of thermoelectric materials. An LSR instrument capable of simultaneously measuring the Seebeck coefficient and electrical resistivity above room temperature was also employed. The carrier concentration of the materials was determined by Hall-effect measurements using the van der Pauw technique in a Physical Properties Measurement System (PPMS) in combination with a Keithley instrument as the current source, an Agilent instrument to measure the voltage, and an HP switch box. A Magnetic Properties Measurement System (MPMS) was used to study all the magnetic properties presented in subsequent chapters.

**Chapter 3:** In this chapter, the thermoelectric properties of a series of GeSe-based-alloys are investigated. GeSe has a layered orthorhombic structure at low temperatures and is known for its ultra-low thermal conductivity. However, the electrical conductivity is too low for thermoelectric applications, even when doped to increase the charge carrier density, due to the relatively large bandgap of this material. Here, we synthesize a series of alloys combining orthorhombic GeSe with cubic $AgBiTe_2$. The alloys crystallize in higher symmetry structures than the pristine orthorhombic structure, decreasing the bandgap and increasing the electrical conductivity. The carrier concentration is significantly increased compared to orthorhombic GeSe. However, the thermal conductivity remains low, resulting in a significant increase in the ZT value.

**Chapter 4:** The breaking of inversion symmetry in layered organic-inorganic perovskite compounds has previously been reported as being due to buckling of the inorganic layer, perhaps involving the Jahn-Teller effect, which leads to an alternating pattern of long and short M-X bond lengths in-plane. Here we show that breaking the inversion symmetry of perovskites based on non-JT-active metal ions is also possible. The inversion symmetry is broken due to the rotational degree of freedom of the organic spacer molecules, which also affects the hydrogen bonding pattern linking the organic and inorganic components and in turn induces buckling of the inorganic layer. We also study the effect of organic cations of different lengths on the two-dimensional magnetic properties.

**Chapter 5:** A large magnetocaloric effect has recently been discovered in certain layered organic-inorganic perovskites. Large magnetic entropy changes that occur on ferromagnetic ordering are behind this effect. Here we report a large magnetoelectric effect in an arylamine-based copper chloride perovskite. The spin ordering in this system can be easily manipulated by an applied

magnetic field, giving rise to a large entropy change. We also investigate the critical behavior close to the magnetic ordering temperature and find it to be consistent with a two-dimensional system.

**Chapter 6:** The optoelectronic properties of hybrid perovskites are known to be tunable by inducing vacancies on the cation and/or anion sites. Here we show that by varying the anion concentration during the synthesis, single crystals with different colour can be obtained. We study the effect of the anion vacancies on the structural and magnetic properties, and also cast doubt on previous studies that suggest both high-spin and low-spin polymorphs of certain hybrid perovskites can be obtained.

## 1.4 References


1 J. C. Blancon, J. Even, C. C. Stoumpos, M. G. Kanatzidis and A. D. Mohite, *Nat. Nanotechnol.*, 2020, **15**, 969–985.

2 L. Mao, C. C. Stoumpos and M. G. Kanatzidis, *J. Am. Chem. Soc.*, 2019, **141**, 1171–1190.

3 L. Hao, D. Meyers, H. Suwa, J. Yang, C. Frederick, T. R. Dasa, G. Fabbris, L. Horak, D. Kriegner, Y. Choi, J.-W. Kim, D. Haskel, P. J. Ryan, H. Xu, C. D. Batista, M. P. M. Dean and J. Liu, *Nat. Phys.*, 2018, **14**, 806–810.

4 A. Shafique and Y. H. Shin, *Sci. Rep.*, 2017, **7**, 506.

5 M. Samanta, T. Ghosh, S. Chandra and K. Biswas, *J. Mater. Chem. A*, 2020, **8**, 12226–12261.

6 N. Sethulakshmi, A. Mishra, P. M. Ajayan, Y. Kawazoe, A. K. Roy, A. K. Singh and C. S. Tiwary, *Mater. Today*, 2019, **27**, 107–122.

7 L. Pedesseau, D. Sapori, B. Traore, R. Robles, H. H. Fang, M. A. Loi, H. Tsai, W. Nie, J. C. Blancon, A. Neukirch, S. Tretiak, A. D. Mohite, C. Katan, J. Even and M. Kepenekian, *ACS Nano*, 2016, **10**, 9776–9786.

8 C. Katan, N. Mercier and J. Even, *Chem. Rev.*, 2019, **119**, 3140–3192.

9 Q. Chen, N. De Marco, Y. (Michael) Yang, T.-B. Song, C.-C. Chen, H. Zhao, Z. Hong, H. Zhou and Y. Yang, *Nano Today*, 2015, **10**, 355–396.

10 J. Hu, L. Yan and W. You, *Adv. Mater.*, 2018, **30**, 1802041.

11 M. D. Smith, B. A. Connor and H. I. Karunadasa, *Chem. Rev.*, 2019, **119**, 3104–3139.

12 D. M. Rowe, Thermoelectric Handbook: From Macro to Nano, CRC Press, 2006.

13 T. M. Tritt, *Annu. Rev. Mater. Res.*, 2011, **41**, 433–448.

14 E. . Snyder, G.J., Toberer, *Nat. Mater.*, 2008, **7**, 105–114.

15 X. Zhou, Y. Yan, X. Lu, H. Zhu, X. Han, G. Chen and Z. Ren, *Mater. Today*, 2018, **21**, 974–988.

16 G. Tan, L. D. Zhao and M. G. Kanatzidis, *Chem. Rev.*, 2016, **116**, 12123–12149.

17 J. He and T. M. Tritt, *Science*, 2017, **357**, 1369–1375.

18 Y. Pei, X. Shi, A. Lalonde, H. Wang, L. Chen and G. J. Snyder, *Nature*, 2011, **473**, 66–69.

19 Y. Pei, A. D. Lalonde, N. A. Heinz, X. Shi, S. Iwanaga, H. Wang, L. Chen and G. J. Snyder, *Adv. Mater.*, 2011, **23**, 5674–5678.

20 Q. Zhang, H. Wang, W. Liu, H. Wang, B. Yu, Q. Zhang, Z. Tian, G. Ni, S. Lee, K. Esfarjani, G. Chen and Z. Ren, *Energy Environ. Sci.*, 2012, **5**, 5246–5251.

21 J. P. Heremans, V. Jovovic, E. S. Toberer, A. Saramat, K. Kurosaki, A. Charoenphakdee, S. Yamanaka and G. J. Snyder, *Science*, 2008, **321**, 554–557.

22 Y. Pei, H. Wang and G. J. Snyder, *Adv. Mater.*, 2012, **24**, 6125–6135.

23 J. P. Heremans, V. Jovovic, E. S. Toberer, A. Saramat, K. Kurosaki, A. Charoenphakdee, S. Yamanaka and G. J. Snyder, *Science.*, 2008, **321**, 1457–1461.

24 M. S. Dresselhaus, G. Chen, M. Y. Tang, R. Yang, H. Lee, D. Wang, Z. Ren, J. P. Fleurial and P. Gogna, *Adv. Mater.*, 2007, **19**, 1043–1053.

25 Y. Pei, N. A. Heinz, A. LaLonde and G. J. Snyder, *Energy Environ. Sci.*, 2011, **4**, 3640-3645.

26 Y. Pei, J. Lensch-Falk, E. S. Toberer, D. L. Medlin and G. J. Snyder, *Adv. Funct. Mater.*, 2011, **21**, 241–249.

27 O. Delaire, J. Ma, K. Marty, A. F. May, M. A. McGuire, M. H. Du, D. J. Singh, A. Podlesnyak, G. Ehlers, M. D. Lumsden and B. C. Sales, *Nat. Mater.*, 2011, **10**, 614–619.

28 Y. Zhou and L. D. Zhao, *Adv. Mater.*, 2017, **29**, 1702676.

29 G. Qin, Z. Qin, W. Z. Fang, L. C. Zhang, S. Y. Yue, Q. B. Yan, M. Hu and G. Su, *Nanoscale*, 2016, **8**, 11306–11319.

30 C. W. Li, J. Hong, A. F. May, D. Bansal, S. Chi, T. Hong, G. Ehlers and O. Delaire, *Nat. Phys.*, 2015, **11**, 1063–1069.

31 L. D. Zhao, S. H. Lo, Y. Zhang, H. Sun, G. Tan, C. Uher, C. Wolverton, V. P. Dravid and M. G. Kanatzidis, *Nature*, 2014, **508**, 373–377.

32 A. Gschneidner, V. K. Pecharsky and A. O. Tsokol, *Reports Prog. Phys.*, 2005, **68**, 1479–1539.

33 K. G. Sandeman, *Scr. Mater.*, 2012, **67**, 566–571.

34 V. K. Pecharsky and K. A. Gschneidner, *J. Magn. Magn. Mater.*, 1999, **200**, 44–56.

35 W. D. van Amstel and L. J. de Jongh, *Solid State Commun.*, 1972, **11**, 1423–1429.

36 Y. Kimishima, *J. Magn. Magn. Mater.*, 1990, **90–91**, 301–302.

37 T. Yoshinari, *Phase Transitions*, 1990, **28**, 79–97.

38 S.-H. Park, I.-H. Oh, S. Park, Y. Park, J. H. Kim and Y.-D. Huh, *Dalt. Trans.*, 2012, **41**, 1237–1242.

39 D. Nafday, D. Sen, N. Kaushal, A. Mukherjee and T. Saha-Dasgupta, *Phys. Rev. Res.*, 2019, **1**, 032034(R).

40 K. W. Lee, C. H. Lee, C. E. Lee and J. Kang, *Phys. Rev. B*, 2000, **62**, 95–98.

41 M. D. Smith, E. J. Crace, A. Jaffe and H. I. Karunadasa, *Annu. Rev. Mater. Res.*, 2018, **48**, 111–136.

42 J. B. Goodenough, *Phys. Rev.*, 1955, **100**, 564–573.

43 J. B. Goodenough, *J. Phys. Chem. Solids*, 1958, **6**, 287–297.

44 J. Kanamori, *J. Phys. Chem. Solids*, 1959, **10**, 87–98.

45 B. Saparov and D. B. Mitzi, *Chem. Rev.*, 2016, **116**, 4558–4596.

46 H. Preier, *Semicond. Sci. Technol.*, 1990, **5**, S12–S20.

47 R. J. Korkosz, T. C. Chasapis, S. H. Lo, J. W. Doak, Y. J. Kim, C. I. Wu, E. Hatzikraniotis, T. P. Hogan, D. N. Seidman, C. Wolverton, V. P. Dravid and M. G. Kanatzidis, *J. Am. Chem. Soc.*, 2014, **136**, 3225–3227.

48 L. Fu, M. Yin, D. Wu, W. Li, D. Feng, L. Huang and J. He, *Energy Environ. Sci.*, 2017, **10**, 2030–2040.

49 T. Ikeda, L. A. Collins, V. A. Ravi, F. S. Gascoin, S. M. Haile and G. J. Snyder, *Chem. Mater.*, 2007, **19**, 763–767.

50 L. D. Zhao, H. J. Wu, S. Q. Hao, C. I. Wu, X. Y. Zhou, K. Biswas, J. Q. He, T. P. Hogan, C. Uher, C. Wolverton, V. P. Dravid and M. G. Kanatzidis, *Energy Environ. Sci.*, 2013, **6**, 3346-3355.

51 Y. Pei, Z. M. Gibbs, A. Gloskovskii, B. Balke, W. G. Zeier and G. J. Snyder, *Adv. Energy Mater.*, 2014, **4**, 1400486.

52 E. K. Chere, Q. Zhang, K. Dahal, F. Cao, J. Mao and Z. Ren, *J. Mater. Chem. A*, 2016, **4**, 1848–1854.

53 M. Gharsallah, F. Serrano-Sánchez, N. M. Nemes, F. J. Mompeán, J. L. Martínez, M. T. Fernández-Díaz, F. Elhalouani and J. A. Alonso, *Sci. Rep.*, 2016, **6**, 26774.

54 Z. Wang, C. Fan, Z. Shen, C. Hua, Q. Hu, F. Sheng, Y. Lu, H. Fang, Z. Qiu, J. Lu, Z. Liu, W. Liu, Y. Huang, Z.-A. Xu, D. W. Shen and Y. Zheng, *Nat. Commun.*, 2018, **9**, 47.

55 C. L. Chen, H. Wang, Y. Y. Chen, T. Day and G. J. Snyder, *J. Mater. Chem. A*, 2014, **2**, 11171–11176.

56 J. E. Boschker, R. Wang and R. Calarco, *CrystEngComm*, 2017, **19**, 5324–5335.

57 J. Li, Z. Chen, X. Zhang, Y. Sun, J. Yang and Y. Pei, *NPG Asia Mater.*, 2017, **9**, e353-8.

58 D. Wu, L.-D. Zhao, S. Hao, Q. Jiang, F. Zheng, J. W. Doak, H. Wu, H. Chi, Y. Gelbstein, C. Uher, C. Wolverton, M. Kanatzidis and J. He, *J. Am. Chem. Soc.*, 2014, **136**, 11412–11419.

59 I. Chowdhury, R. Prasher, K. Lofgreen, G. Chrysler, S. Narasimhan, R. Mahajan, D. Koester, R. Alley and R. Venkatasubramanian, *Nat. Nanotechnol.*, 2009, **4**, 235–238.

60 O. Eibl, K. Nielsch, N. Peranio and F. Volklein, *Thermoelectric Bi2Te3 Nanomaterials*, Wiley, 2015.

61 H. Wang, Z. M. Gibbs, Y. Takagiwa and G. J. Snyder, *Energy Environ. Sci.*, 2014, **7**, 804–811.

62 S. Lee, K. Esfarjani, T. Luo, J. Zhou, Z. Tian and G. Chen, *Nat. Commun.*, 2014, **5**, 3525.

63 M. D. Nielsen, V. Ozolins and J. P. Heremans, *Energy Environ. Sci.*, 2013, **6**, 570–578.

64 J. P. Heremans, *Nat. Phys.*, 2015, **11**, 990–991.

65 M. Cagnoni, D. Führen and M. Wuttig, *Adv. Mater.*, 2018, **30**, 1801787.

66 G. Ding, G. Gao and K. Yao, *Sci. Rep.*, 2015, **5**, 9567.

67 S. Hao, F. Shi, V. P. Dravid, M. G. Kanatzidis and C. Wolverton, *Chem. Mater.*, 2016, **28**, 3218–3226.

68 S. Roychowdhury, M. Samanta, S. Perumal and K. Biswas, *Chem. Mater.*, 2018, **30**, 5799–5813.

69 S.-D. Guo and Y.-H. Wang, *J. Appl. Phys.*, 2017, **121**, 034302.

70 X. Zhang, J. Shen, S. Lin, J. Li, Z. Chen, W. Li and Y. Pei, *J. Mater.*, 2016, **2**, 331–337.

71 L. Shaabani, S. Aminorroaya-Yamini, J. Byrnes, A. Akbar Nezhad and G. R. Blake, *ACS Omega*, 2017, **2**, 9192–9198.

72 E. M. Levin, M. F. Besser and R. Hanus, *J. Appl. Phys.*, 2013, **114**, 083713.

73 P. B. Littlewood, *J. Phys. C Solid State Phys.*, 1980, **13**, 4855–4873.

74 T. Zhu, Y. Yang, K. Gu, C. Liu, J. Zheng and X. Gong, *ACS Appl. Mater. Interfaces*, 2020, **12**, 51744–51755.

75 L. Piveteau, V. Morad and M. V. Kovalenko, *J. Am. Chem. Soc.*, 2020, **142**, 19413–19437.

76 F. Zhang, H. Lu, J. Tong, J. J. Berry, M. C. Beard and K. Zhu, *Energy Environ. Sci.*, 2020, **13**, 1154–1186.

77 B. Sun, X.-F. Liu, X.-Y. Li, Y. Zhang, X. Shao, D. Yang and H.-L. Zhang, *Chem. Mater.*, 2020, **32**, 8914–8920.

78 S. Ma, M. Cai, T. Cheng, X. Ding, X. Shi, A. Alsaedi, T. Hayat, Y. Ding, Z. Tan and S. Dai, *Sci. China Mater.*, 2018, **61**, 1257–1277.

79 G. Grancini and M. K. Nazeeruddin, *Nat. Rev. Mater.*, 2019, **4**, 4–22.

80 Z. Cheng and J. Lin, *CrystEngComm*, 2010, **12**, 2646–2662.

81 B. Huang, B. Y. Wang, Z. Y. Du, W. Xue, W. J. Xu, Y. J. Su, W. X. Zhang, M. H. Zeng and X. M. Chen, *J. Mater. Chem. C*, 2016, **4**, 8704–8710.

82 X. Li, B. Li, J. Chang, B. Ding, S. Zheng, Y. Wu, J. Yang, G. Yang, X. Zhong and J. Wang, *ACS Appl. Energy Mater.*, 2018, **1**, 2709–2716.

83 S. Y. Kim, J. M. Yang, E. S. Choi and N. G. Park, *Adv. Funct. Mater.*, 2020, **30**, 2002653.

84 S. Zhao, C. Lan, H. Li, C. Zhang and T. Ma, *J. Phys. Chem. C*, 2020, **124**, 1788–1793.

85 T. Niu, Q. Xue and H.-L. Yip, *Nanophotonics*, 2021, **10**, 2069–2102.

86 D. Ghosh, D. Acharya, L. Pedesseau, C. Katan, J. Even, S. Tretiak and A. J. Neukirch, *J. Mater. Chem. A*, 2020, **8**, 22009–22022.

87 W. K. Lee, *J. Chem. Phys.*, 1996, **104**, 6964–6966.

88 G. Heger, D. Mullen and K. Knorr, *Phys. Stat. Sol A.*, 1976, **35**, 627–637.

89 R. Mokhlisse, M. Couzi and J. C. Lassegues, *J. Phys. C Solid State Phys.*, 1983, **16**, 1353–1366.

90 T. Ishihara, J. Takahashi and T. Goto, *Phys. Rev. B*, 1990, **42**, 11099–11107.

91 X. Gong, O. Voznyy, A. Jain, W. Liu, R. Sabatini, Z. Piontkowski, G. Walters, G. Bappi, S. Nokhrin, O. Bushuyev, M. Yuan, R. Comin, D. McCamant, S. O. Kelley and E. H. Sargent, *Nat. Mater.*, 2018, **17**, 550–556.

92 A. Fieramosca, L. Polimeno, V. Ardizzone, L. De Marco, M. Pugliese, V. Maiorano, M. De Giorgi, L. Dominici, G. Gigli, D. Gerace, D. Ballarini and D. Sanvitto, *Sci. Adv.*, 2019, **5**, eaav9967.

93 Y. Zhai, S. Baniya, C. Zhang, J. Li, P. Haney, C. X. Sheng, E. Ehrenfreund and Z. V. Vardeny, *Sci. Adv.*, 2017, **3**, e1700704.

94 I. H. Park, Q. Zhang, K. C. Kwon, Z. Zhu, W. Yu, K. Leng, D. Giovanni, H. S. Choi, I. Abdelwahab, Q. H. Xu, T. C. Sum and K. P. Loh, *J. Am. Chem. Soc.*, 2019, **141**, 15972–15976.

95 S. Wang, X. Liu, L. Li, C. Ji, Z. Sun, Z. Wu, M. Hong and J. Luo, *J. Am. Chem. Soc.*, 2019, **141**, 7693–7697.

96 L. J. de Jongh, A. C. Botterman, F. R. de Boer and A. R. Miedema, *J. Appl. Phys.*, 1969, **1363**, 5–8.

97 H. Tsai, W. Nie, J. C. Blancon, C. C. Stoumpos, R. Asadpour, B. Harutyunyan, A. J. Neukirch, R. Verduzco, J. J. Crochet, S. Tretiak, L. Pedesseau, J. Even, M. A. Alam, G. Gupta, J. Lou, P. M. Ajayan, M. J. Bedzyk, M. G. Kanatzidis and A. D. Mohite, *Nature*, 2016, **536**, 312–317.

98 M. Yuan, L. N. Quan, R. Comin, G. Walters, R. Sabatini, O. Voznyy, S. Hoogland, Y. Zhao, E. M. Beauregard, P. Kanjanaboos, Z. Lu, D. H. Kim and E. H. Sargent, *Nat. Nanotechnol.*, 2016, **11**, 872–877.

99 L. Li, Z. Sun, P. Wang, W. Hu, S. Wang, C. Ji, M. Hong and J. Luo, *Angew. Chemie - Int. Ed.*, 2017, **56**, 12150–12154.

100 Y. H. Kim and N. Hur, *J. Korean Phys. Soc.*, 2020, **77**, 1026–1030.

101 B. Kundys, A. Lappas, M. Viret, V. Kapustianyk, V. Rudyk, S. Semak, C. Simon and I. Bakaimi, *Phys. Rev. B*, 2010, **81**, 224434.

102 B. Huang, J. Y. Zhang, R. K. Huang, M. K. Chen, W. Xue, W. X. Zhang, M. H. Zeng and X. M. Chen, *Chem. Sci.*, 2018, **9**, 7413–7418.

103 X. Han, Y. Zheng, S. Chai, S. Chen and J. Xu, *Nanophotonics*, 2020, **9**, 1787–1810.